Cationic Surface Reconstructions on Cerium Oxide Nanocrystals: An Aberration-Corrected HRTEM Study

Umananda M. Bhatta,[†] Ian M. Ross,[‡] Thi X. T. Sayle,[§] Dean C. Sayle,[§] Stephen C. Parker,[⊥] David Reid,[∥] Sudipta Seal,[∥] Amit Kumar,[∥] and Günter Möbus[†,*]

[†]Department of Materials Science and Engineering, University of Sheffield, Sheffield, S1 3JD, U.K., [‡]Department of Electronic and Electric Engineering, University of Sheffield, Sheffield, S1 3JD, U.K., [§]Department Engineering and Applied Science, Cranfield University, Defense Academy of the U.K., Shrivenham, Swindon, SN6 8LA, U.K., [⊥]Department Chemistry, University of Bath, Claverton Down, Bath, Avon, BA2 7AY, U.K., and [∥]Advanced Materials Processing Analysis Center (AMPAC) and Nanoscience Technology Center (NSTC), Mechanical Materials and Aerospace Engineering, University of Central Florida, Florida 32816, United States

ABSTRACT Instabilities of nanoscale ceria surface facets are examined on the atomic level. The electron beam and its induced atom migration are proposed as a readily available probe to emulate and quantify functional surface activity, which is crucial for, for example, catalytic performance. *In situ* phase contrast high-resolution transmission electron microscopy with spherical aberration correction is shown to be the ideal tool to analyze cationic reconstruction. Hydrothermally prepared ceria nanoparticles with particularly enhanced {100} surface exposure are explored. Experimental analysis of cationic reconstruction is supported by molecular dynamics simulations where the Madelung energy is shown to be directly related to the binding energy, which enables one to generate a visual representation of the distribution of "reactive" surface oxygen.

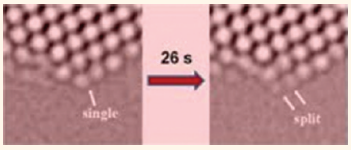

KEYWORDS: nanoparticles · surface reconstruction · atomic hopping · ceria · Madelung energy

Compounds that can be reduced or oxidized easily, such as ceria, have found applications as catalysts in vehicle emission control systems and electrolyte materials in solid oxide fuel cells.[1,2] The catalytic activity of cerium oxide originates from surface oxygen, and so it is important to increase the active surface area in order to obtain enhanced catalytic activity. There have been several successful attempts to fabricate ceria of reduced size, thereby increasing the surface area to maximize catalytic activity.[3] The presence of such reactive oxygen species and oxygen storage capacity (OSC) would also play a crucial role in some other important applications such as antioxidants in the biomedical field.[4,5] In order to use cerium oxide effectively in all the above applications, it is important that we understand the behavior and activity of oxygen, the distribution of vacancies, and the defect structure and defect mobility at the surface of the cerium oxide nanoparticle. Another alternative way to enhance OSC would be to tune the morphology of the cerium oxide nanoparticles such that the most reactive surfaces are more exposed. Thus, there have been several successful attempts to increase the OSC and catalytic efficiency by changing the morphology of ceria, to maximize {100} exposure.[6−8]

There are several molecular modeling studies exploring the relative stabilities of different crystalline surfaces.[9−12] The catalytic activity and mobility of Ce and O ions on the surface of ceria nanoparticles are linked with how strongly each atom is bound to the surface. Now it is well established that the binding energy of the atoms on the low-index surfaces follows the order {111} > {110} > {100}. Calculating the binding energy of atoms on the surface of a ceria nanoparticle is straightforward.[13] However, undertaking such calculations for all surface atoms is computationally expensive. Recently, Migani and co-workers showed that the "oxygen vacancy formation energy is driven by the electrostatics",[14] thus enabling the prediction of the most easily removable O atoms by analyzing the distribution of the electrostatic potential in the pristine stoichiometric (vacancy-free) ceria systems. Accordingly, the Madelung energy, calculated for each atom, will provide insight into how strongly each atom is bound to the surface and therefore a reflection of its relative mobility and reactivity compared to other ions. Here, we use atomistic computer simulations to generate models for ceria nanoparticles and predict their surface reactivity by calculating the Madelung energies of the atoms.

* E-mail: g.moebus@sheffield.ac.uk.

Received for review October 1, 2011 and accepted December 13, 2011.

Published online December 13, 2011
10.1021/nn2037576

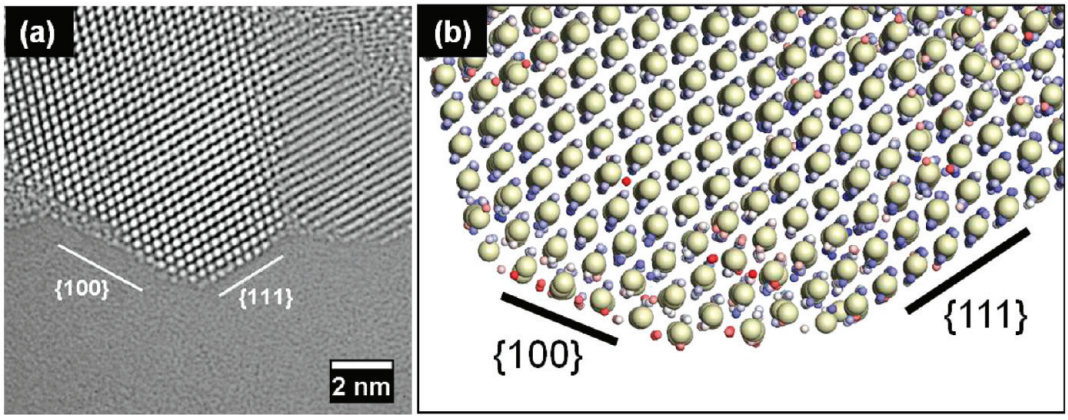

Figure 1. (a) Faceted ceria nanoparticle imaged along the [110] zone axis using 300 kV JEM-3100 R005 aberration-corrected TEM showing {111} and {100} facets. The image, taken at slight underfocus, has been black-white inverted for better visibility of atomic columns. (b) Atomistic model revealing {100} and {111} surfaces to compare with experiment. Cerium positions are represented by large spheres, and oxygen positions represented by small spheres colored according to Madelung energy (red = low, blue = high).

Even though techniques such as XRD and XPS have been found suitable for studying changes in lattice constants of nanocrystals accompanied by a change in oxidation states,[15,16] high-resolution TEM accompanied with associated techniques (electron diffraction, EELS, STEM, *etc.*) can reveal local changes in the surfaces of nanostructures down to atomic resolution[17] and has been used effectively for nonoxide materials as well.[18,19] Here we aim at analyzing relative stabilities and levels of reconstruction of {111} and {100} surfaces of hydrothermally produced cerium oxide nanocrystals,[7] which were found to have more {100} exposed surfaces by means of aberration-corrected HRTEM.

RESULTS

The hydrothermally fabricated material is found to consist of a high proportion of cuboid particles, making this powder industrially relevant with respect to catalytic applications. A faceted cerium oxide nanoparticle was selected and imaged such that we can clearly see an extended {100} surface adjoining a smaller {111} surface (Figure 1a). To clarify the geometry and crystallography, the experimental image is set next to a molecular dynamics simulated system showing the same joining interfaces (Figure 1b), which will assist in the interpretation of findings (see Discussion section). Dynamic changes under the e-beam were observed by taking a series of 30 images at an interval of 2 s each (Figure 2). It is important to note that the changes were not triggered by a focused beam; the condenser was simply adjusted to illuminate a region larger than the CCD camera field of view to get a high enough signal-to-noise ratio in the image series. It is confirmed that atomic motion happens across the wide {100} face, extending our earlier findings for octahedral ceria crystals,[20] where these motions were confined to one tiny {100}-type facet of the capped octahedron, which is stabilized by suppressing the octahedral corner. In the present study, our aim is to measure atomic motion as well as reconstruction of the terminating monolayer in extended surfaces of both {100} and {111} type, which must be stabilized intrinsically, and compare the relative stability of the two different surfaces.

In a first qualitative evaluation we aim to classify patterns of atomic movements. At first line profiles through the outermost four monolayers along each of the two surface directions are plotted as a function of time with the image intensity as ordinate, indicating changes in the number of atoms on each peak with increasing irradiation (Figure 3). Along {111} the length of the line selected for the profile plot is about 5.0 nm, and along {100}, 6.1 nm. The first four rows are referred to as $\{111\}_1$ $\{111\}_2$ $\{111\}_3$ $\{111\}_4$ and $\{100\}_1$ $\{100\}_2$ $\{100\}_3$ $\{100\}_4$, respectively.

Evaluation of {111} Surface. Over the 60 s no ablation of atoms is visible; all movements appear reversible and random. If we look at row 1 closely, some positions even increase over time (*e.g.*, 4 and 6), while others fluctuate between two levels (*e.g.*, 1, 2, 3, 7, and 9). For example, changes of up to 10% of maximum intensity, corresponding to purple-blue color changes (position 3, row1) in Figure 3, occur. Spatially, atomic motion is stronger on the left, near the corner of {100}, than on the right. Profiles for the inner three rows appear quite stable, as expected with $\{111\}_4$ (which serves as our noise estimate to separate real hopping processes from random intensity fluctuations). Several positions as a function of time seem to zigzag, suggesting that apart from hopping from one row to another, whole columns of atoms perpendicular to the plane of the image also move in random directions. This makes it difficult to quantitatively measure the number of atoms joining or leaving a particular position.

Evaluation of the Corner of {111}/{100}. An illustrative example of the unpredictable nature of atomic hopping is the corner formed by $\{100\}_2$ and $\{111\}_1$. This single

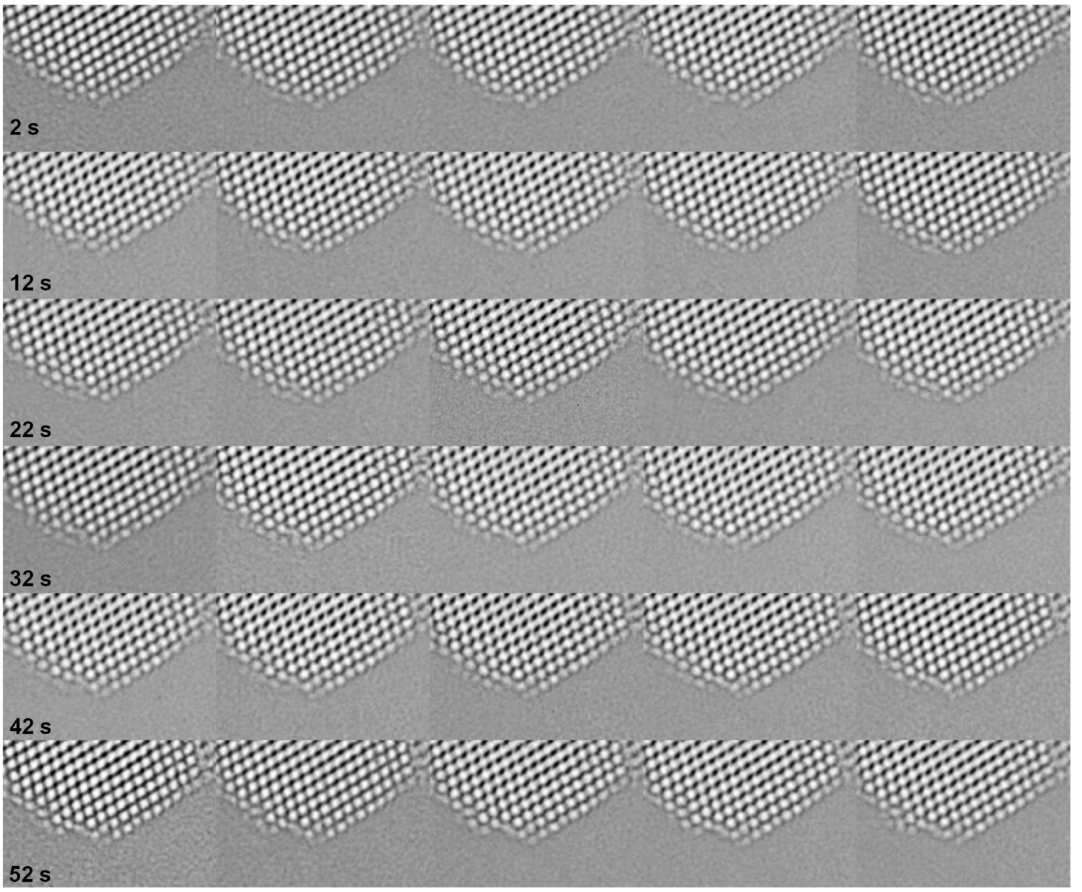

Figure 2. Time series of atomic hopping processes on a ceria nanoparticle, recorded at a time interval of 2 s (imaging conditions as with Figure 1a).

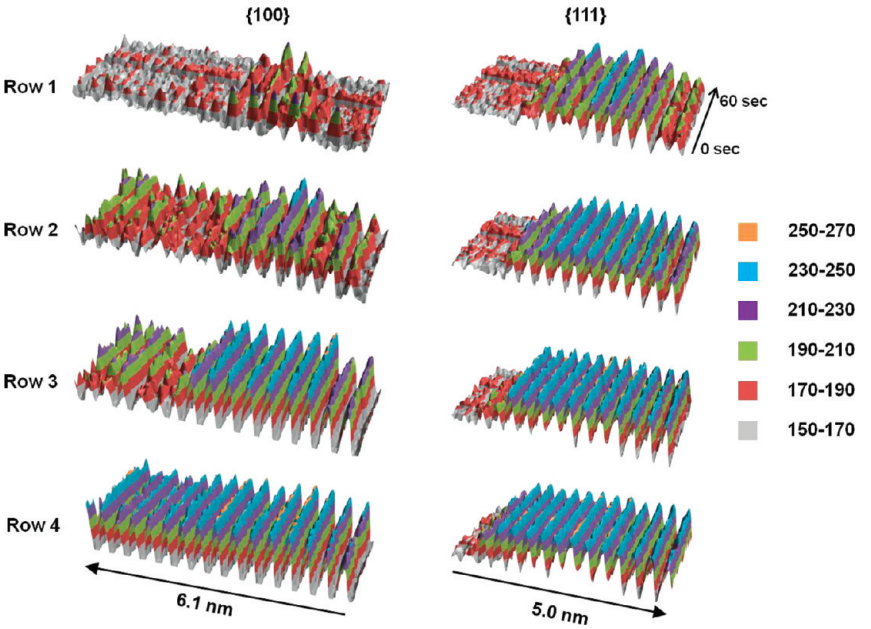

Figure 3. Intensity 3D surface plots of profiles of the first four rows along {100} and {111}, respectively. Color-intensity conversion table is at the right.

crystallographic Ce site appears to fluctuate between a single elliptically smeared out atomic spot, a sharp single atomic spot, and two almost separate spots (Figure 4). In detail, the elliptical spot (2 s) turns into a

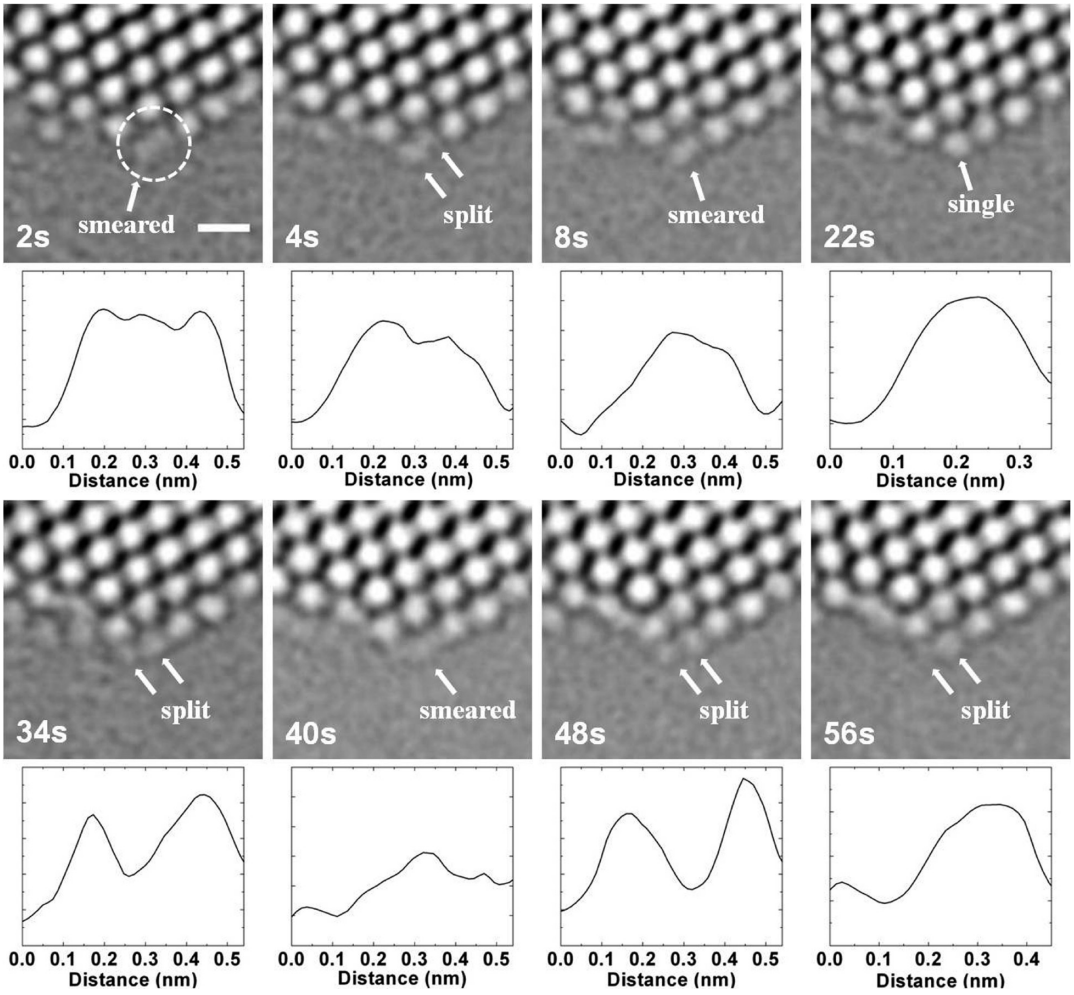

Figure 4. Magnified images of the {100}/{111} corner region in selected time frames. Below: profile plots through the reconstructing Ce-corner-site, demonstrating major changes in positions, occupancy, and Ce–Ce projected neighbor distances. Scale bar = 0.5 nm.

split spot (4 s) with both subspots being displaced from their nearest crystallographic Ce site, and after further fluctuations at 22 s a bright single position can be seen. After 34 s another positional split appears (see also the profile plot), now opening (temporarily only) a new corner site (Pos 1 along $\{100\}_1$, however inward relaxed).

Evaluation of {100} Surface. Line profiles of Figure 3 immediately indicate the huge increase in hopping activity whenever Ce is free to move at the top, which includes the full $\{100\}_1$, the left seven positions of $\{100\}_2$, and even some $\{100\}_3$ sites close to the {111} facet. As a selected example, the third, fourth, and fifth positions in $\{100\}_1$ (from right) are found to be particularly active. These activities affect the number of atoms in the immediate neighborhood (*i.e.*, third position from right in $\{100\}_2$); see Figure 3. Another high activity example is the left-hand side of the $\{100\}_2$ and $\{100\}_3$ rows, which look displaced and very mobile, being partially exposed surfaces.

The most striking evidence of cationic surface reconstruction appears at Pos 6 along $\{100\}_1$, where two image spots occupy one bulk Ce site for most of the time series. Therefore atom oscillations during one 2 s exposure time can be excluded in favor of lasting cationic surface reconstruction, while oxygen does not contribute significantly to image contrast. Figure 5 magnifies the region around Pos 6 along with horizontal intensity profiles through the reconstructed sites. Of the split spots, one subspot, best seen as Pos 6_1 in Figure 5c, is located close to the projected octahedral interstitial sites in the fluorite unit cell, while both spots are displaced from bulk positions.

Quantification of Hopping Activity *via* Cross-Correlation. It is valuable to assign a single number to each layer at/below a surface facet of a nanocrystal, which describes the relative activity, comprising atom number fluctuations in a column or lateral movements through dynamic relaxations and reconstructions.

First, we propose to quantify inter- and intra-column/row hopping of atoms *via* the cross-correlation function between two consecutive images of rows:

$$\mathrm{xcf} = \frac{\sum (A_i - \langle A \rangle) \cdot (B_i - \langle B \rangle)}{\sqrt{\sum (A_i - \langle A \rangle)^2} \cdot \sqrt{\sum (B_i - \langle B \rangle)^2}} \qquad (1)$$

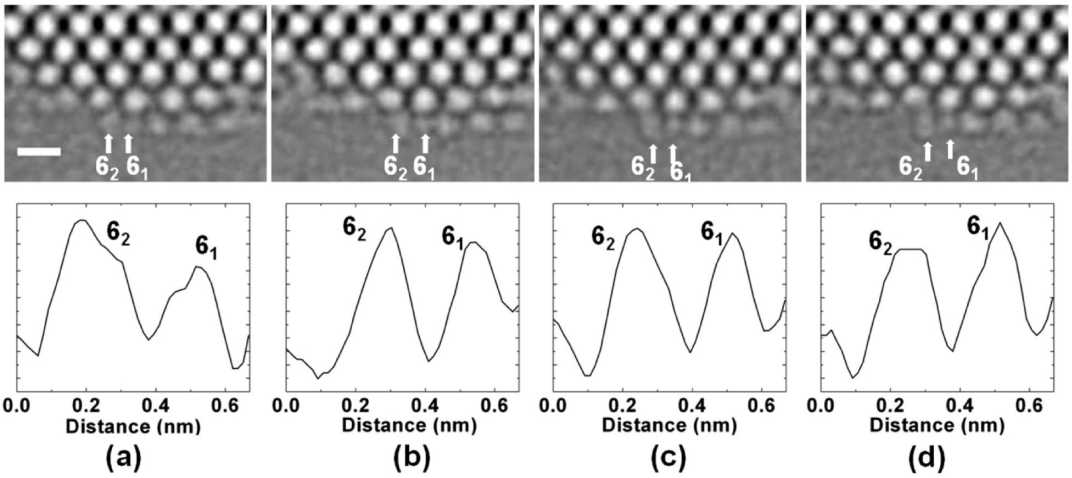

Figure 5. Magnified images of the {100} surface of Figure 1, opposite the corner region of Figure 4. Below: profile plots of layer $\{100\}_1$, lattice position 6 (counted from the right), corresponding to (a) 20 s, (b) 30 s, (c) 32 s, and (d) 34 s, illustrating the two spots labeled 6_1 and 6_2, which are part of a surface reconstruction with two projected atomic spots occupying one bulk lattice Ce site. Scale bar = 0.5 nm.

A and B represent profile plots for two consecutive frames separated by 2 s: $B = A+2$ s, while i runs along all the pixels along the length of the profile of rows $\{111\}_1$, $\{111\}_2$, $\{100\}_1$, and $\{100\}_2$. The 30 available frames over 60 s allow calculating xcf functions for 29 pairs of A,B for a given row. The average of those 29 xcf's for each row gives clear quantitative evidence as to which row/facet is more active. According to these calculations, $\{111\}_2$ has a value of 0.95, which is a bit higher compared to 0.94 obtained for $\{111\}_1$, as it is protected by the top layer. Overall the xcf values for {100} planes are lower compared to their {111} counterparts: xcf's for $\{100\}_1$ and $\{100\}_2$ were found to be 0.83 and 0.91, respectively. Most significantly $\{100\}_1$ is much lower than the {111} equivalent, indicating high instability along this surface. Thus the above-defined parameter proves to be a suitable parameter to quantify surface instability and functional surface activity.

Quantification of Lattice Dynamics *via* Interatomic Distance Measurements. Another way of quantifying the amount of surface reconstruction and its dynamics near the surface is by measuring the changes in atomic column positions. Figure 6 represents average interatomic distances of all the positions for the first two rows along each facet {111} and {100} plotted against their interatomic positions d_{ij}, with d_{ij} representing the distance between pos i and pos j, $j = i + 1$. For example, d_{12} along $\{111\}_1$ was measured for all 30 frames taken over 60 s and averaged. The deviation from the mean value is shown as an "error bar", which actually is a measure of the true amplitude of atom movements/atom relaxations over time. The same procedure was repeated for all the available consecutive positions along a given row and then for other rows alike. Again, the first two positions that are closer to the active {100} surface, d_{12} and d_{23}, fluctuate more compared with the rest of the interatomic distances, indicating overspill from {100}. The corner positions $\{100\}_1$ and $\{100\}_2$ are expected to be the most active region, and they show not only the largest fluctuations but also the largest absolute interatomic distances, both proving their major deviation from bulk crystallography.

Image Simulation. To confirm the interpretation of atomic spots with Ce atomic columns, HRTEM image simulations were employed using Java EMS software[21,22] for a range of defocus values starting from −25 to +25 nm in steps of 5 nm and varying thickness. Two regions of interest, A and B, on Figure 7a are matched with simulations for a thickness of 1.5 and 8.5 nm, respectively (Figure 7b and c). Slight differences between experimental and simulated parts can be attributed to a possible mis-tilt in the projection of the CeO_2 crystal. Ce columns are black in the original image, as in Figure 6, and turn white after contrast inversion in Figures 1 and 2. For zero spherical aberration we suppress visibility of the disturbing carbon support film, which is a weak phase object, while maximizing the heavy amplitude-phase contrast of Ce.

Molecular Modeling. The atomistic structure of a particular CeO_2{100} surface is shown in Figure 8a and reveals that the surface atomic layer comprises −Ce−O−Ce−O− chains. This change of stoichiometry from CeO_2 to CeO_1 facilitates quenching of the dipole associated with fluorite {100} surfaces.[23] In Figure 8b, the Madelung energy of the oxygen ions in the −Ce−O−Ce−O− chain are shown and reveal that the oxygen ions comprising the chain have low Madelung energies, and therefore we predict they are more mobile compared with oxygen comprising other sites, such as {111}. Inspection of the model simulated under MD simulation performed at high temperature reveals that the oxygen ions at {100} are indeed highly mobile. Moreover, the atoms do not move in an autonomous

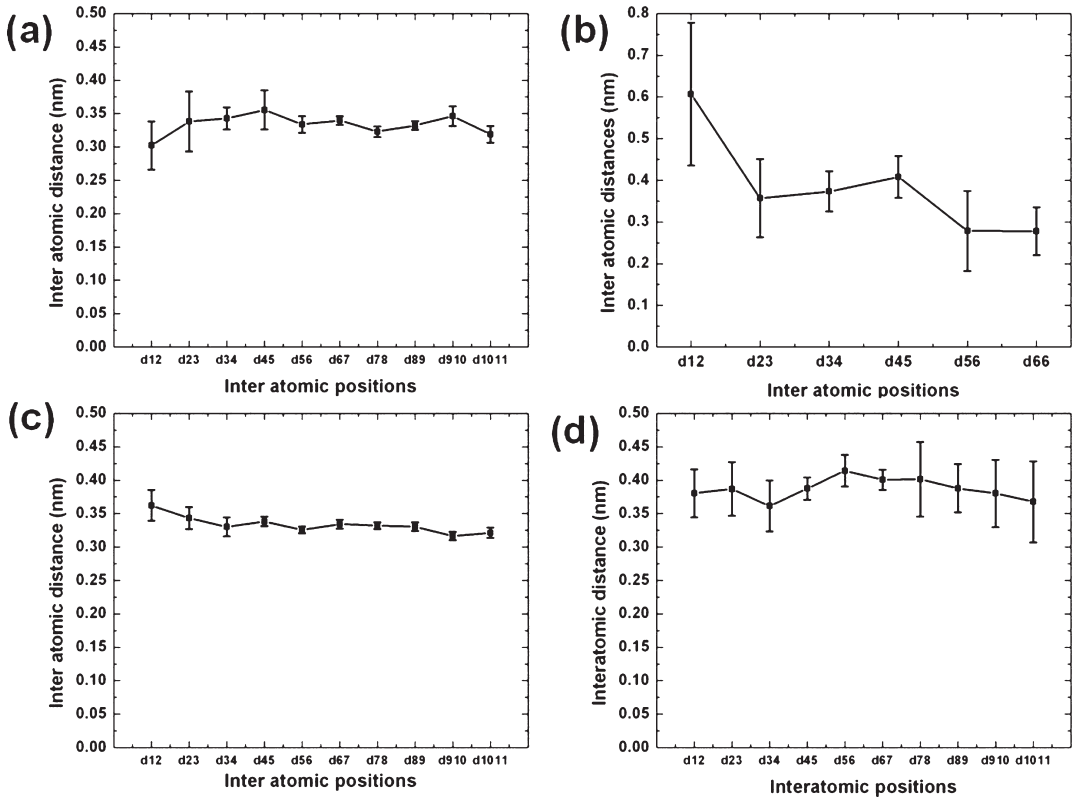

Figure 6. Average projected interatomic distances, plotted as a function of their corresponding positions d_{ij} ($j = i + 1$) along (a) $\{111\}_1$, (b) $\{100\}_1$, (c) $\{111\}_2$, and (d) $\{100\}_2$. The error bars represent the true measure of amplitude of atom movements/atom relaxations over time.

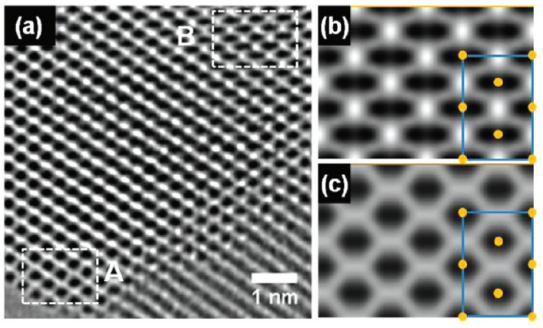

Figure 7. Experimental (a) contrast details (magnified from Figure 2, $t = 2$s) with matching HRTEM image simulations (b, c) for two crystal regions near the surface and in the nanoparticle interior (1.5 and 8.5 nm thickness). Unit cell and Ce column positions are indicated, JEOL JEM 3100 R005, $C_s = 0$.

fashion; rather the −Ce−O−Ce−O− chains move as a whole, analogous to the movement of a snake.

DISCUSSION

Cationic surface reconstruction on ceria has not been observed before, mainly due to the fact that information about the atomic structure of Ce {111} and {100} surfaces has been reported only by scanning tunneling microscopy (STM) and scanning force microscopy (SFM). STM {111} studies revealed the presence of surface defects predominantly consisting of triangular oxygen vacancy defects at room temperature.[24,25] On the other hand, SFM studies, apart from showing similar triangular oxygen defects, also give useful information on characteristics of terraces, step edges, kinks, and pits on the Ce{111} surfaces, which is directly related to its ability to adsorb CO and other catalytic activities.[26−28] For {100}, according to Nörenberg and Harding,[23] a (3×2)45°-type reconstruction is found in the terminating oxygen layer.

Unlike HRTEM, SPM measurements are performed on extended (semi-infinite) crystals, and the Tasker classification[29] applies, with fluorite {111} being a stable type II, and fluorite {100} an unstable type III, surface with intrinsic dipole moment. For nanoparticles, it is to be noted that finite size effects restrict the energy penalty for type III infinite crystals. Also the electron beam induced oxygen ablation under prolonged irradiation could render the fluorite {111} surface Ce terminated, which is another unstable type III surface, which could explain some atomic motion observed. Evidently, cationic surface reconstruction would be triggered by creation of oxygen vacancies at the surface, which influence the atoms/atomic columns present at the exposed surface to occupy interstitial positions during the course of e-beam exposure. Further significant oxygen loss, such as inside the $\{100\}_1$ layer in Figure 5, at the start of irradiation would open up the space that allows Ce interstitial positions to emerge.

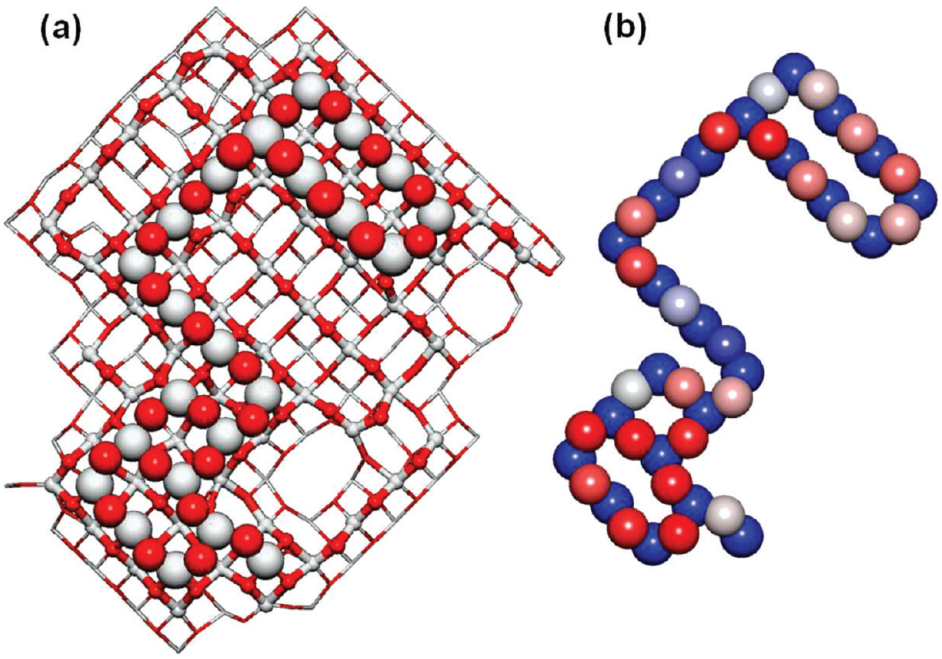

Figure 8. (a) Atomistic structure of a {100} surface revealing the −Ce−O−Ce−O−Ce− chains on the surface atomic layer, which evolve to help quench the surface dipole associated with fluorite {100}; penultimate surface atoms are represented by ball-and-stick and the layer below using a stick model representation. (b) Surface atomic layer of the −Ce−O−Ce−O−Ce− chain; oxygen is represented by spheres colored according to Madelung energy (red = low, blue = high), and cerium atoms are represented by blue spheres. (See Supporting Information for images of the full crystal models.)

In TEM we can dynamically observe Ce atomic motions, but the actual imaging of oxygen vacancies and defects at the surface is difficult.

As mentioned earlier, a measure of the ease of oxygen extraction from the surface of ceria is directly related to its catalytic reactivity.[9] The mobility of ions and ease of oxygen extraction from a particular surface are dependent upon the Madelung energy. Our calculations reveal that the Madelung energies of oxygen on {100} are generally much lower compared with oxygen on {111} surfaces. Accordingly the simulations predict that oxygen on {100} will be more mobile and easier to extract, compared to oxygen on {111}. Our experiments reveal, in accord with our simulations, a much higher mobility for ions comprising CeO_2{100} compared with {111}. Accordingly, because the Madelung energy links mobility and reactivity, we argue that the ionic mobility, observed experimentally, can be used as a direct measure of reactivity. With the help of molecular dynamics simulation, we confirmed that the energetically most favorable structure corresponds to a Ce−O stoichiometry with both oxygen and Ce missing compared to the bulk structure. This reconstruction quenches the dipole moment and brings the overall {100} surface energy closer to the {111} level, and could therefore explain why ceria cuboid crystals with extended {100} faces exist in the first place. The direction and length of the CeO chains are randomly distributed and considered highly mobile; their total occupancy corresponds to only 50% oxygen. Our cross-sectional surface views of ceria {100} surfaces and their dynamics support the theoretical model, by the observation that entire atomic columns move within a 2 s interval to a neighboring position.[20]

An important question is whether the limited lateral extent (nanosize effects) of our facets, in comparison to infinite surfaces normally used in STM studies, influences the {100} surface reconstructions and any associated changes in ion mobility To explore this issue, we analyzed various models of ceria nanoparticles and nanorods with exposed {100} surfaces (Figure 9). Analysis, using molecular graphical techniques, of all the nanoceria {100} surfaces revealed significant surface reconstruction with characteristic −Ce−O−Ce−O−Ce−O− chain structures, which enable surface dipole quenching. We note that the detailed atomistic structure can change slightly between {100} surfaces exposed. However, the size of the surface and architecture of the nanostructure appear not to govern the "chain" configuration and hence reactivity. The technique of simulated amorphization and crystallizion[30,31] was used to generate the atomistic models of nanoceria. Accordingly, the area of {100} surfaces exposed by the (model) nanoceria is dependent upon the crystallization. Similar to the experiment, the simulator can exact control only over the crystallization conditions of temperature and pressure and not structure. For this reason, the atomistic structures of the {100} surfaces in Figure 9 are subtly different. Nanomaterial synthesis necessarily involves a crystallization step. By simulating, in part, the synthetic process, we argue that our models are more representative of real

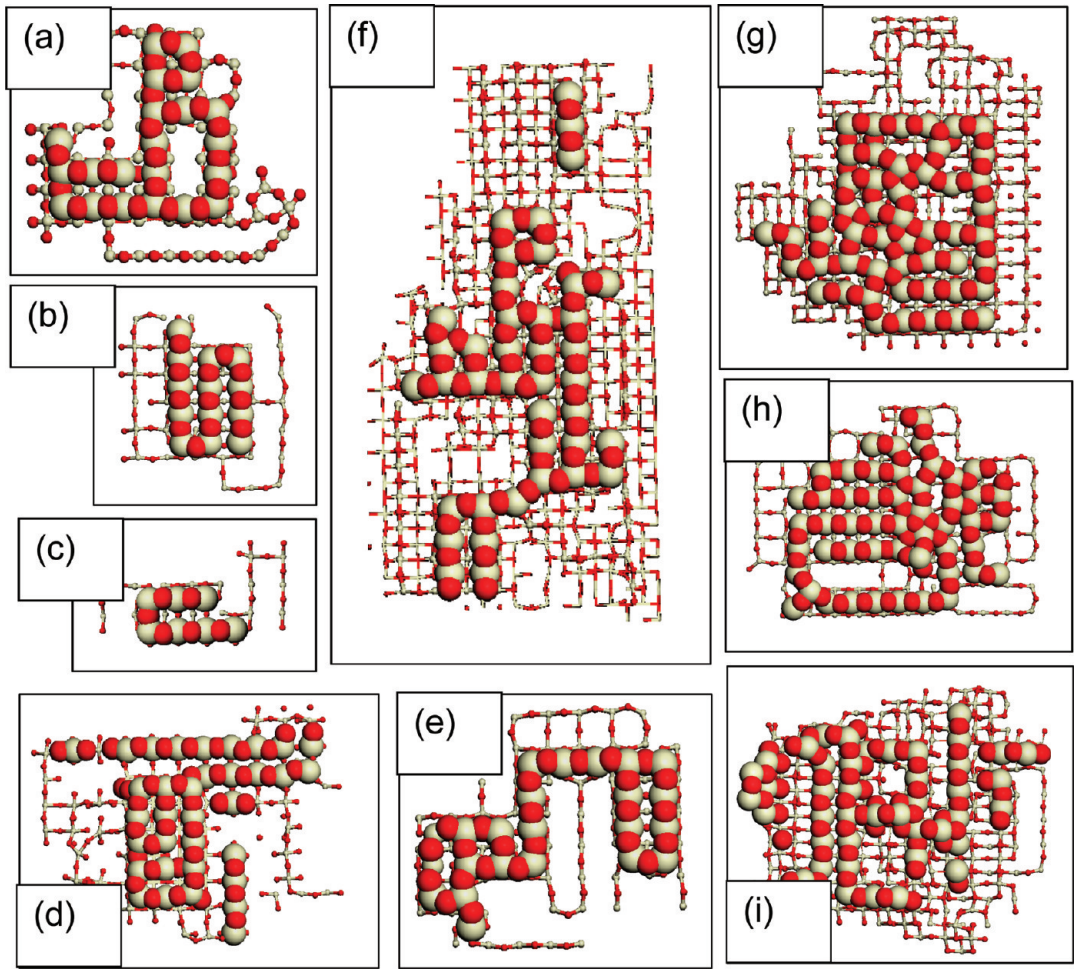

Figure 9. Atomistic structure of CeO_2 {100} surfaces. (a–e) {100} surfaces of a nanoparticle of ceria comprising 24 696 atoms; (f) nanorod with (110) growth direction; (g, h) nanoparticle comprising 15 972 atoms; (i) nanorod with (211) growth direction. The atom positions comprising the top atomic layer are represented by large spheres; a ball-and-stick model is used to represent atom positions below the top layer. To preserve clarity of the figure, the remaining atom positions are not shown. Cerium is colored white and oxygen is red.

nanoceria, compared with models generated "by hand" using, for example, symmetry operators; the simulation strategies used to generate the models of ceria nanoparticles and nanorods are available in refs 30 and 31.

Oxidation state measurements on various ceria nanoparticles have been carried out before,[15–17] with the surface found enriched in Ce^{3+} and the particle interior being pure Ce^{4+}. However, the main message of our work is that the surface activity cannot be characterized by simple valence measurements and derived proportions of oxygen deficiency corresponding to a ratio for Ce:O of 1/2 (CeO_2) to 2/3 (Ce_2O_3). Only atomic reconstruction and atomic surface mobility including local temporary stoichiometries of <2/3 (such as Ce–O) are able to describe the complete picture.

CONCLUSIONS

The characterization of ceria surfaces by cross-sectional views of an aberration-corrected HRTEM image time series allowed us to perform several innovative examinations and deduce relevant conclusions for both basic surface science and industrial applications:

- Unlike SPM, XPS, or other surface science techniques, we can characterize precisely indexed nanofacets of individual nanocrystals, thereby avoiding averaging of properties over different surface indices or differently shaped crystals.
- We have documented extensive cerium atomic hopping movements now for the first time observed on laterally extended {100} surfaces and to a smaller degree on {111} surfaces after variable times of irradiation. Therefore we can exclude less important corner effects as the exclusive cause of such motion, previously observed on tiny cap-facets on octahedral nanoparticles, and predict the high surface activity of our hydrothermally produced cuboid particles with maximized exposure of {100} faces. These particles are of primary importance for practical applications, and our results are therefore far-ranging beyond surface science theory.

- We propose two quantitative parameters, both derivable from HRTEM images by image processing, that are suitable to quantify atomic hopping activity and in proportion functional surface activity (as would, for example, dictate the catalytic efficiency) for each facet and each monolayer in each facet individually. Both cross-correlation of direct image intensity profiles and standard deviations of atomic position fluctuations are found to be suitable parameters and proportional to each other. We therefore propose considering electron-beam-triggered surface reconstruction and atomic motion as an ultrahigh-resolution probe to measure important surface characteristics of immediate industrial relevance.
- We observe cationic surface reconstruction in some areas near corners or steps of {100} surfaces, with Ce atom columns splitting, such that two spots occupy one bulk Ce site, with one subspot possibly adopting an octahedral interstitial site. This is related to oxygen ablation beyond the traditional level of reduction to Ce^{3+} and could be helpful for future predictions of surface rearrangements under chemically triggered reactions, other than by electron beam. Surface reconstruction of {100} into linear CeO chains is found by molecular dynamics surface relaxation and supported by observation of hopping events involving entire columns of atoms. From a theory point of view, examination of nanoparticles by HRTEM allows studying the existence of systems without infinite surface energy unlike for bulk/semi-infinite systems.
- The oxidative catalytic activity of CeO_2 nanoparticles is ultimately related to the ease of oxygen extraction from the surface. One can predict whether surface oxygen sites are active by calculating the binding energy associated with the oxygen. That the Madelung energy is directly related to the binding energy enables one to generate a visual representation of the distribution of "reactive" surface oxygen and hence the oxygen storage capacity with direct implications for catalysis, antioxidants. Simulations can help rationalize the mobility of ions on the surface of ceria nanoparticles.

METHODS

Preparation of Ceria Nanoparticles. *Materials and Synthesis.* Cerium nitrate hexahydrate (99.999% purity, Sigma Aldrich) was dissolved in deionized (DI) water. In a separate beaker sodium hydroxide (Sigma Aldrich) was dissolved in DI water. Both solutions were stirred for 30 min and then mixed together and stirred for three hours. On immediate mixing, the color of the solution was light yellow and later changed to purple. The reaction mixture was hydrothermally treated in Teflon-lined stainless steel autoclaves for 48 h at a temperature of 160 °C. The sample was taken out after the hydrothermal treatment and washed thoroughly with DI water until the pH is near neutral. The washing procedure was to stir the solution in DI water for 30 min and then centrifuged at 10 000 rpm for 10 min. The final solution was dried at 300 °C for two hours.

TEM Measurements. Aberration-corrected TEM (Sheffield JEM 3100 R005) at 300 kV with spherical aberration close to zero and near Gaussian focus has been used, as the suppression of amorphous carbon film background by vanishing weak-phase contrast was crucial in maximizing atomic resolution visibility of cerium, which itself due to its high atomic number generates contrast by a mixture of amplitude and phase contrast. Standard imaging conditions for the JEM R005 TEM with second condenser aperture and a spot size of one were used. Two-fold and 3-fold astigmatism were corrected to below 7 and 70 nm, respectively. Residual spherical aberration was estimated to 0.5 μm. Image series were automatically acquired in 2 s intervals using a Gatan Ultrascan 2k×2k camera. Gatan Digital Micrograph and ImageJ software were used for postprocessing of the images.

Atomistic Modeling. Atomistic models of CeO_2 nanoparticles were generated using simulated amorphization and crystallization; full details of this method, together with the potential models used to describe ceria, can be found elsewhere, and therefore only salient details are provided here.[30,31] In particular, two cubes of CeO_2 comprising 15 972 and 24 696 atoms were cleaved from the parent material. Each system was then melted, by performing high-temperature Molecular Dynamics (MD) simulation using the DL_POLY[32] code, and then crystallized by performing MD simulation at reduced temperatures. During the crystallization step crystalline seeds, conforming to the fluorite crystal structure, evolved spontaneously within the amorphous sea of ions. The seeds then nucleated the crystallization of the remaining amorphous ions. The Madelung energies of each atom comprising the nanoparticles were then calculated using METADISE.[33]

Acknowledgment. We thank EPSRC, UK, for funding the microscopy and modeling parts (EP/H001298 and EP/H001220) as well as NSF NIRT for Nanoceria research (NSF International supplement: CBET 1028996).

Supporting Information Available: High-resolution image simulations of ceria along the [110] zone axis and a molecular modeling of the structure of a ceria nanoparticle are provided complementary to Figures 7 and 8, respectively. Also an animation sequence in avi format showing the atomic hopping is provided. This material is available free of charge via the Internet at http://pubs.acs.org.

REFERENCES AND NOTES

1. Trovarelli, A. *Catalysis By Ceria and Related Materials*, 2nd ed.; Imperial College Press: London, 2002.
2. Chao, C. C.; Hsu, C. M.; Cui, Y.; Prinz, F. B. Improved Solid Oxide Fuel Cell Performance with Nanostructured Electrolytes. *ACS Nano* **2011**, *5*, 5692–5696.
3. Masui, T.; Fujiwara, K.; Machida, K.; Adachi, G. Characterization of Cerium (IV) Oxide Ultrafine Particles Prepared Using Reversed Micelles. *Chem. Mater.* **1997**, *9*, 2197–2204.
4. Schubert, D.; Dargusch, R.; Raitano, J.; Chan, S. W. Cerium and Yttrium Oxide Nanoparticles are Neuroprotective. *Biochem. Biophys. Res. Commun.* **2006**, *342*, 86–91.
5. Celardo, I.; Nicola, M. D.; Mandoli, C.; Pedersen, J. Z.; Traversa, E.; Ghibelli, L. Ce^{3+} Ions Determine Redox-Dependent Anti-Apoptotic Effect of Cerium Oxide Nanoparticles. *ACS Nano* **2011**, *5*, 4537–4549.
6. Skorodumova, N. V.; Baudin, M.; Hermansson, K. Surface Properties of CeO_2 from First Principles. *Phys. Rev. B* **2004**, *69*, 075401–8.
7. Mai, H. X.; Sun, L. D.; Zhang, Y.-W.; Si, R.; Feng, W.; Zhang, H.-P.; Liu, H.-C.; Yan, C.-H. Shape-Selective Synthesis and

Oxygen Storage Behavior of Ceria Nanopolyhedra, Nanorods, and Nanocubes. *J. Phys. Chem. B* **2005**, *109*, 24380–24385.
8. Zhou, K.; Wang, X.; Sun, X.; Peng, Q.; Li, Y. Enhanced Catalytic Activity of Ceria Nanorods from Well-Defined Reactive Crystal Planes. *J. Catal.* **2005**, *229*, 206–212.
9. Sayle, T. X. T.; Parker, S. C.; Catlow, C. R. A. The Role of Oxygen Vacancies on Ceria Surfaces in the Oxidation of Carbon Monoxide. *Surf. Sci.* **1994**, *316*, 329–336.
10. Inoue, T.; Ohashi, M.; Sakamoto, M.; Shida, S. Orientation Selective Epitaxial Growth of CeO Image Layers on Si(100) Substrates Using Reactive DC Magnetron Sputtering with Substrate Bias. *J. Cryst. Growth* **2004**, *271*, 176–183.
11. Sayle, D. C.; Maicaneanu, S. A.; Watson, G. W. Atomistic Models for CeO_2(111), (110), and (100) Nanoparticles, Supported on Yttrium-Stabilized Zirconia. *J. Am. Chem. Soc.* **2002**, *124*, 11429–11439.
12. Conesa, J. C. Computer Modeling of Surfaces and Defects on Cerium Dioxide. *Surf. Sci.* **1995**, *339*, 337–352.
13. Sayle, T. X. T.; Parker, S. C.; Sayle, D. C. Oxidising CO to CO_2 Using Ceria Nanoparticles. *Phys. Chem. Chem. Phys.* **2005**, *7*, 2936–41.
14. Migani, A.; Vayssilov, G. N.; Bromley, S. T.; Illas, F.; Neyman, K. M. Dramatic Reduction of the Oxygen Vacancy Formation Energy in Ceria Particles: A Possible Key to Their Remarkable Reactivity at the Nanoscale. *J. Mater. Chem.* **2010**, *20*, 10535–10546.
15. Tsunekawa, S.; Fukuda, T.; Kasuya, A. X-ray Photoelectron Spectroscopy of Monodisperse CeO_{2-x} Nanoparticles. *Surf. Sci.* **2000**, *457*, L437–L440.
16. Zhang, F.; Chan, S. W.; Spanier, J. E.; Apak, E.; Jin, Q.; Robinson, R. D.; Herman, I. P. Cerium Oxide Nanoparticles: Size-Selective Formation and Structure Analysis. *Appl. Phys. Lett.* **2002**, *80*, 127–129.
17. Wu, L.; Wiesmann, H. J.; Moodenbaugh, A. R.; Klie, R. F.; Zhu, Y.; Welch, D. O.; Suenaga, M. Oxidation State and Lattice Expansion of CeO_{2-x} Nanoparticles As a Function of Particle Size. *Phys. Rev. B* **2004**, *69*, 125415.
18. Kisielowski, C.; Freitag, B.; Bischoff, M.; van Lin, H.; Lazar, S.; Knippels, G.; Tiemeijer, P.; van der Stam, M.; von Harrach, S.; Stekelenburg, M.; *et al*. Detection of Single Atoms and Buried Defects in Three Dimensions by Aberration-Corrected Electron Microscope with 0.5-Å Information Limit. *Microsc. Microanal.* **2008**, *14*, 469–477.
19. Hetherington, C. J. D.; Chang, L. Y. S.; Haigh, S.; Nellist, P. D.; Gontard, L. C.; Dunin-Borkowski, R. E.; Kirkland, A. I. High-Resolution TEM and the Application of Direct and Indirect Aberration Correction. *Microsc. Microanal.* **2008**, *14*, 60–67.
20. Möbus, G.; Saghi, Z.; Sayle, D. C.; Bhatta, U. M.; Stringfellow, A.; Sayle, T. X. T. Dynamics of Polar Surfaces on Ceria Nanoparticles Observed *In-situ* with Single-Atom resolution. *Adv. Funct. Mater.* **2011**, *21*, 1971–1976.
21. Stadelmann, P. Effect of Three-Fold Astigmatism on High Resolution Electron Micrographs. *Ultramicroscopy* **1995**, *60*, 103–113.
22. http://cimewww.epfl.ch/people/stadelmann/jemsWebSite/jems.html.
23. Nörenberg., H.; Harding, J. H. The Surface Structure of CeO_2(0 0 1) Single Crystals Studied by Elevated Temperature STM. *Surf. Sci.* **2001**, *477*, 17–24.
24. Nörenberg., H.; Briggs, G. A. D. Defect Structure of Non-stoichiometric CeO_2(111) Surfaces Studied by Scanning Tunneling Microscopy. *Phys. Rev. Lett.* **1997**, *79*, 4222–4225.
25. Nörenberg., H.; Briggs, G. A. D. Defect Formation on CeO_2(111) Surfaces after Annealing Studied by STM. *Surf. Sci. Lett.* **1999**, *424*, L32.
26. Torbrügge, S.; Cranney, M.; Reichling, M. Morphology of Step Structures on CeO_2(111). *Appl. Phys. Lett.* **2008**, *73*, 073112–3.
27. Gritschneder, S.; Namai, Y.; Iwasawa, Y.; Reichling, M. Structural Features of CeO_2(111) Revealed by Dynamic SFM. *Nanotechnology* **2005**, *16*, S41–S48.
28. Gritschneder, S.; Reichling, M. Structural Elements of CeO_2-(111) Surfaces. *Nanotechnology* **2007**, *18*, 044024–9.
29. Tasker, P. W. The Stability of Ionic Crystal Surfaces. *J. Phys. C: Solid State Phys.* **1977**, *12*, 4977–4984.
30. Feng, X. D.; Sayle, D. C.; Wang, Z. L.; Paras, M. S.; Santora, B.; Sutorik, A. C.; Sayle, T. X. T.; Yang, Y.; Ding, Y.; Wang, X. D.; Her, Y. S. Converting Ceria Polyhedral Nanoparticles into Single-Crystal Nanospheres. *Science* **2006**, *312*, 1504–1508.
31. Sayle, D. C.; Feng, X.; Ding, Y.; Wang, Z. L.; Sayle, T. X. T. "Simulating Synthesis": Ceria Nanosphere Self-Assembly into Nanorods and Framework Architectures. *J. Am. Chem. Soc.* **2007**, *129*, 7924–7935.
32. www.cse.clrc.ac.uk/msi/software/DL_POLY/.
33. Watson, G. W.; Kelsey, E. T.; deLeeuw, N. H.; Harris, D. J.; Parker., S. C. Atomistic Simulation of Dislocations, Surfaces and Interfaces in MgO. *J. Chem. Soc., Faraday Trans.* **1996**, *92*, 433–438.